ADVANCED MATERIALS INTERFACES
Open Access
www.advmatinterfaces.de

Contact Geometry and Pathway Determined Carriers Transport through Microscale Perovskite Crystals

Zhibin Zhao, Yuelong Li, Lifa Ni, Jongwoo Nam, Adila Adijiang, Xubin Zhang, Shanshan Li, Mingwei Wang, Takhee Lee, and Dong Xiang**

With the miniaturization of crystals-based photoelectric devices, electrode contact-geometries may play a critical role in determining the device performance. However, investigation of the role of electrode contact geometries in situ faces great challenges due to the electrode contact geometry is typically unmodifiable. To this end, a kind of liquid metal is employed as an adaptive-deformable electrode to study the carrier transport through perovskite microcrystals, in which the electrode contacts geometries/positions and thus the carrier-pathways can be adjusted. Under light illumination, a spike feature of photocurrent is observed when carriers transport along the perovskite microcrystal surface upon an edge-contact geometry, which is absent as the carrier mainly transport through crystal interior upon a top-contact geometry. Switching, rectifying, and memristor functions are selectively realized just by modifying the contact geometry. The underlying mechanism for the observations is further elucidated. This study provides a platform for studying carrier transport through microscale crystals with adjustable contact geometry and supplies an approach for fabricating diverse functional devices by changing the electrode contact-geometries.

1. Introduction

The metal halide perovskites, particularly $MAPbX_3$ (MA = methylammonium and X = Cl, Br, or I), have attracted tremendous attention in the past decade due to their unique electronic/optical properties and promising applications in many fields.[1–9] Among all of their intriguing properties, ion migration is considered to be an important factor responsible for many anomalies that are observed in perovskite materials and devices, including current–voltage hysteresis,[10] self-healing,[11] switchable photovoltaic effects,[12] large dielectric constants,[13] phase separation,[14,15] and negative differential resistance.[16] Solid evidence also shows that ion migration in perovskites can cause degradation of solar cells[17–19] and low-efficiency light emission.[20–23] Therefore, it is essential to fully understand the properties of ion migration in perovskite materials. However, the relation between ion migration and the electrode contact geometry had not yet been addressed to the best of our knowledge.

One of the important factors which determined ion migration is the distribution of defects along the carrier transport pathway.[24] Due to the presence of unsaturated chemical bonds,[25] charge accumulation,[26] surface strain,[27] hydration,[28] chemical impurities,[29] etc., the defect density near the single crystal surface is normally higher than that inside the crystal interior. Ion migration and trapping/detrapping events influenced by defect distribution will be greatly enhanced when the crystal-size is decreased due to the increased electric field upon a bias and the increased surface-to-volume ratio in the microscale crystal. Accordingly, the electrode geometry and carrier pathway will play a more important role in determining the device performance (such as perovskite solar cells,[30] photodetectors,[31] light-emitting diodes,[32] and resistive switches[33]) as the crystal size is reduced.

To reveal the influence of electrode contact geometry on carrier transport and ions migration in microscale perovskite crystal, liquid-metal Eutectic gallium–indium (EGaIn, a printing ink for electronic circuits) was employed as an adaptive deformable top electrode, in which the electrode contacts geometries and thus the carrier-pathways can be flexibly adjusted via the contact position selection and the force control applied on the electrode.

Z. Zhao, L. Ni, A. Adijiang, X. Zhang, S. Li, M. Wang, D. Xiang
Institute of Modern Optics and Center of Single Molecule Sciences
Key Laboratory of Micro-scale Optical Information Science and Technology
Nankai University
Tianjin 300350, China
E-mail: xiangdongde@nankai.edu.cn

Y. Li
Institute of Photoelectronic Thin Film Devices and Technology
Key Laboratory of Photoelectronic Thin Film Devices and Technology of Tianjin
Solar Energy Research Center
Nankai University
Tianjin 300350, China

J. Nam, T. Lee
Department of Physics and Astronomy, and Institute of Applied Physics
Seoul National University
Seoul 08826, Korea
E-mail: tlee@snu.ac.kr

The ORCID identification number(s) for the author(s) of this article can be found under https://doi.org/10.1002/admi.202202177.

DOI: 10.1002/admi.202202177

ADVANCED MATERIALS INTERFACES
Open Access
www.advmatinterfaces.de

We demonstrated that the electrode geometry (and thus carrier-pathway) not only affects the carrier generation/recombination and trapping/detrapping processes but also strongly influences conductive filament formation assisted by the ion migration in perovskite microcrystals. It was further revealed that different prototype devices (e.g., resistive switches, current rectifiers, and memristors) can be realized just by changing the carrier-pathways with appropriately sized perovskite crystals. Assisted by the systematic measurement with varied bottom electrode materials, photoluminescence spectrum, and X-ray photoelectron spectroscopy, it is concluded that these pathway-determined features originate from the inhomogeneous distribution of defects, that is, defect-assisted ion migration and defects-mediated carrier trapping/detrapping process, which are enhanced by the increased electric field and surface-to-volume ratio in the microscale crystals.

2. Results and Discussion

2.1. Junction Formation and Test Platform

EGaIn is used as a top electrode to reveal the role of the contact-geometry in determining the performance of microscale perovskite crystals with the following advantages: 1) The adaptive deformation of the EGaIn electrode with a soft contact interface guarantees the establishment of a stable/tight contact and provides an adjustable contact area without mechanical damage;[34] 2) Various electrode geometries can be generated and remained via the spontaneously formed ultrathin GaO_x layer on EGaIn surface,[35] making it feasible to adjust the contact geometry/position and thus to mediate carrier-pathway; 3) EGaIn possesses liquid fluidity, self-healing, and high conductivity,[36] enabling it to be used as printing ink and thus provide the potential to integrate perovskite into flexible electronics circuit (e.g., wearable devices and artificial synapses[37,38]).

Correspondingly, a single graphene layer is mainly used as a bottom electrode in our experiments with the following considerations: 1) The atoms in the inactive graphene electrode do not migrate (i.e., the atoms will not escape from the graphene electrode surface) even under a high electric field,[39] so that conductive filaments formation originated from bottom graphene electrode can be high likely excluded; 2) Graphene electrodes array can be generated using standard lithography/etching technique that makes it feasible to fabricate highly integrated devices; 3) The excellent light transmission of graphene make it a promising electrode material for the fabrication of highly efficient solar cells.

Figure 1A illustrates the experimental system for carrier dynamics measurement upon light illumination, which mainly consists of an electrode movement control component, a sensitive current measurement device, and a light source. The top EGaIn tip electrode was generated by stretching a drop of EGaIn (Figure S1 and Video S1, Supporting Information). The curvature of the tip can be adjusted by controlling the stretching speed (Figure S2, Supporting Information) and the adaptive deformation of EGaIn is shown in Video S2, Supporting Information. The bottom graphene electrode was fabricated by transferring single graphene layer onto a SiO_2/Si substrate (Figure S3, Supporting Information). As a supplementary,

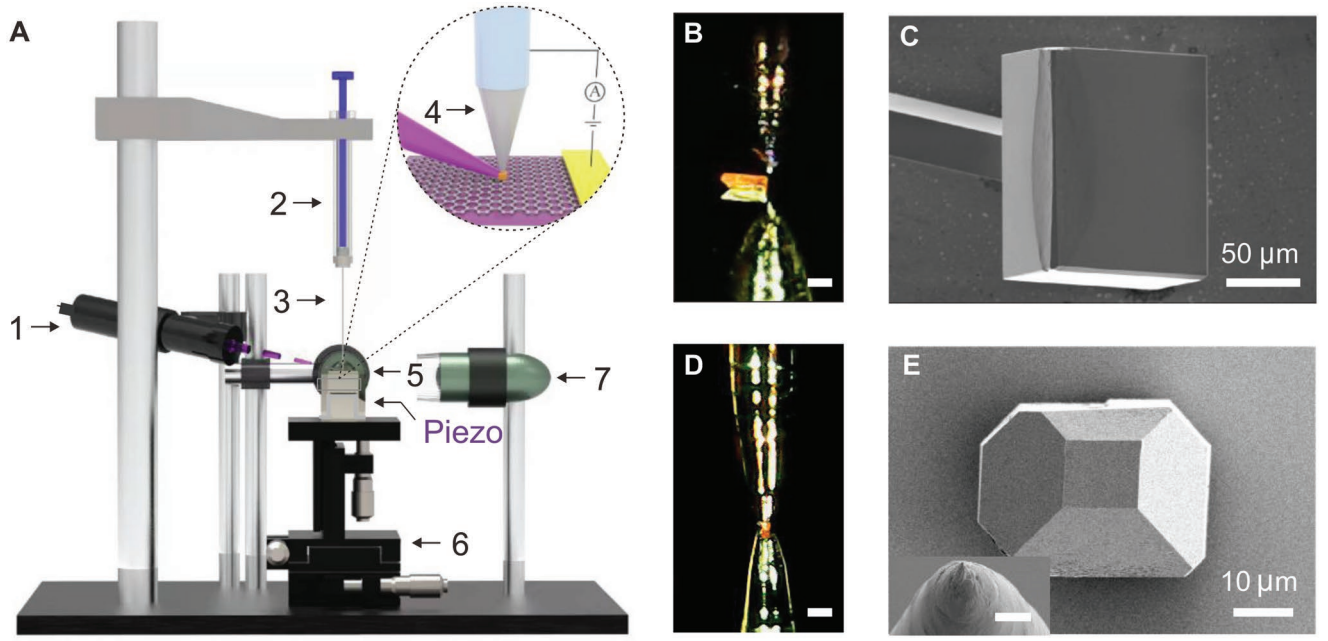

Figure 1. Carrier dynamics measurement system and SEM images of perovskite microcrystals. A) System for the formation of EGaIn–perovskite–graphene junction upon laser illumination. 1: Laser; 2: Syringe; 3: Needle; 4: Top EGaIn electrode; 5: Backside microscope; 6: Displacement platform; 7: Lateral microscope. B) Optical image of the EGaIn–perovskite–graphene junction sandwiched with a large regular perovskite microcrystal. A mirror image of the top EGaIn is observed on the bottom substrate. Scale bar: 50 μm. C) SEM image of the large perovskite microcrystal. D) Optical image of the EGaIn–perovskite–graphene junction sandwiched with a small irregular perovskite microcrystal. Scale bar: 50 μm. E) SEM image of small perovskite microcrystal with polyhedral shape. Insert: SEM image of EGaIn tip with a scale bar of 20 μm.

super-smooth bottom Au (Ag) was also fabricated by peeling the glass chip from the Si wafer (Figure S4, Supporting Information). EGaIn–perovskite–graphene junctions were formed by moving the bottom electrode to approach the top suspended EGaIn electrode via a piezoelectric-driven mechanism. The junction formation is monitored by two mutually orthogonal digital microscopes. A semiconductor laser (λ = 405 nm) with adjustable illumination frequency and controllable power is used as the light source to generate photoexcited carriers.

Figure 1B,D is the optical images of EGaIn–perovskite–graphene junctions with different perovskite crystal sizes, for example, regular quasi-cube ($L \approx 100$ µm in length) as well as irregular quasi-polyhedron ($L \approx 40$ µm in total length), which were mainly studied in the following experiments. And the relatively regular perovskite single crystals with large size are used to form top contact and edge contact, while small irregular single crystals are used to form top contact and half-enclosed contact. Due to the smooth surface of the bottom substrate, a mirror image of the top EGaIn can be observed on the bottom substrate surface. Figure 1C,E present scanning electron microscope (SEM) images of the $MAPbBr_3$ microcrystals with different shapes/sizes, in which clear edges and distinct square corners are observed, indicating the high quality of the perovskite single crystals. The detailed synthesis process and the characterization of the perovskite microcrystals can be found in our previous reports,[40] and more tested microcrystals with varied shapes and sizes can be found in Figure S2, Supporting Information.

2.2. Carrier Dynamics along Different Pathways

Figure 2 shows the photodynamic response of the junctions and the proposed mechanism for the observations as the carrier transport along different pathways upon light illumination. Figure 2A shows the top-contact geometry that the top EGaIn electrode makes a point contact with the center of the top surface of perovskite crystal (so called top-contact geometry). Figure 2B shows that the photocurrent sharply increases to a steady-state upon light illumination and then sharply decreases to nearly zero as the light is turned off with this top-contact geometry. This observation is reasonable since a large number of carriers (electrons and holes) are generated under light illumination and efficiently collected by the biased electrodes, leading to a fast increase of photocurrent (Figure 2C).

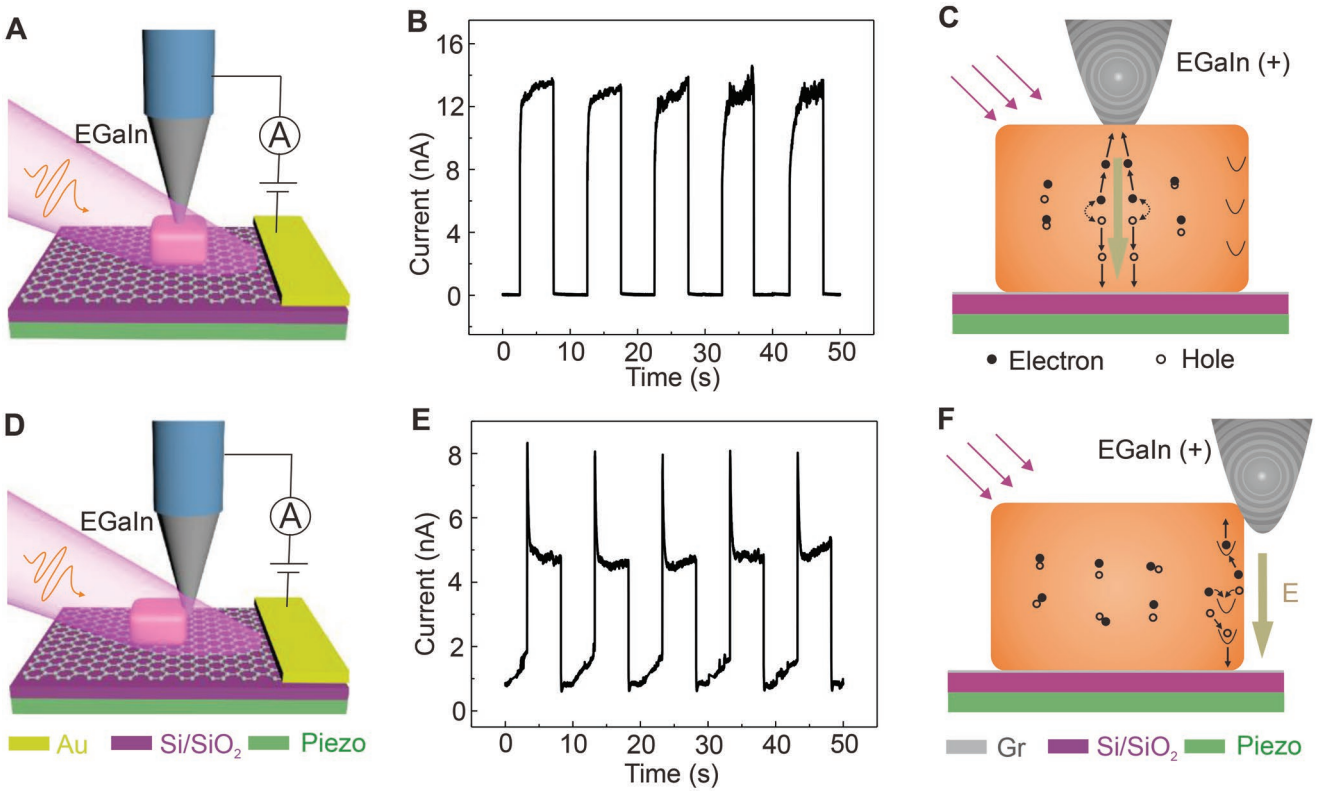

Figure 2. Photodynamic responses of the EGaIn–perovskite–graphene junction upon light illumination with different contact geometries. The length of the perovskite microcrystals is ≈100 µm, the frequency of laser illumination is 0.1 Hz, and the applied voltage is 1.0 V. A) Schematic of the top-contact geometry. B) Photodynamic responses of the junction with the top-contact geometry. The current rises suddenly to a plateau state upon light illumination and decreases to nearly zero as the light is turned off. C) Schematic of the proposed mechanism for the photocurrent response, as presented in (B). Upon light absorption, considerable carriers are generated and efficiently collected by the electrodes, leading to a sudden increase in photocurrent. D) Schematic of the edge-contact geometry. E) Photodynamic responses of the junction upon light illumination for edge-contact geometry. A spike in the current upon light illumination and a slow rise in current upon light shutoff are observed. F) Schematic of the mechanism for the photodynamic response as presented in (E). Carrier transport along crystal surface is mainly dominated by defects assisted carrier generation/recombination and trapping/detrapping process.

Figure 2D shows the schematic of the junctions with an edge contact-geometry, in which the top EGaIn tip makes a point contact with the vertical edge of the perovskite crystal (Video S3, Supporting Information). In this edge-contact geometry, we presume the carriers are mainly transported along the crystal vertical surface since the height of the crystal sidewall results in the shortest distance between the top and bottom electrodes, and the carrier transport always tends to select the shortest path with the lowest resistance. Figure 2E displays the photodynamic response of the junctions with this edge-contact geometry. Contrast to Figure 2B, distinguishable characteristics are observed: 1) The photocurrent increases sharply followed by a decay to a plateau upon light illumination, that is, a spike feature is clearly presented; and 2) the photocurrent declines to a relatively low value rather than nearly zero, and then ascends gradually when the light is turned off, completely different from the observations with top-contact geometry. In addition, it can be found that the top-contact geometry has a relatively larger photocurrent dynamic response compared to the edge-contact geometry. This indicates that to obtain a larger photocurrent, not only the contact area between the top electrode and perovskite should be ensured to realize the effective collection of photogenerated carriers, but also sufficient illuminated area should be ensured to generate enough photogenerated carriers.

The proposed mechanism for this stark discrepancy is presented in Figure 2F. It is known that the defect density on the perovskite surface is higher than that in the perovskite interior.[24,41,42] These defects can act as electron–hole trap centers (or carrier recombination centers), which will result in a rapid decrease of photocurrent upon light illumination as far as carriers transporting along the crystal surface encounter considerable defects. Therefore, a spike feature in the photocurrent will be observed with the edge-contact geometry.[16,43] The defects can not only work as carrier trap centers to trap the carrier upon light illumination, but also detrap/release the carrier as the light is turned off.[44] Accordingly, the carrier detrapping process will slow down the reduction of photocurrent when the light is turned off, which leads to the observation that the photocurrent does not decrease to zero and followed by a slow uptrend.

To address the carrier dynamics response to a continuously varied electric field, a double sweep voltage is applied to the crystal junctions. **Figure 3**A shows the characterizations of carrier transport during the voltage sweep process for the top-contact geometry. A reproducible *S*-shape with slightly asymmetric *I*–*V* curves was observed, implying that injection barriers exist depending on the energy landscape of the junctions. Figure 3B displays the *I*–*V* curves for the edge-contact geometry. It presents significant differences compared to those with the top-contact geometry. At first, the *I*–*V* curves for the edge-contact geometry exhibit obvious Ohmic behavior as shown in segments 2, 3, and 4, indicating that metallic-type highly conducting paths are

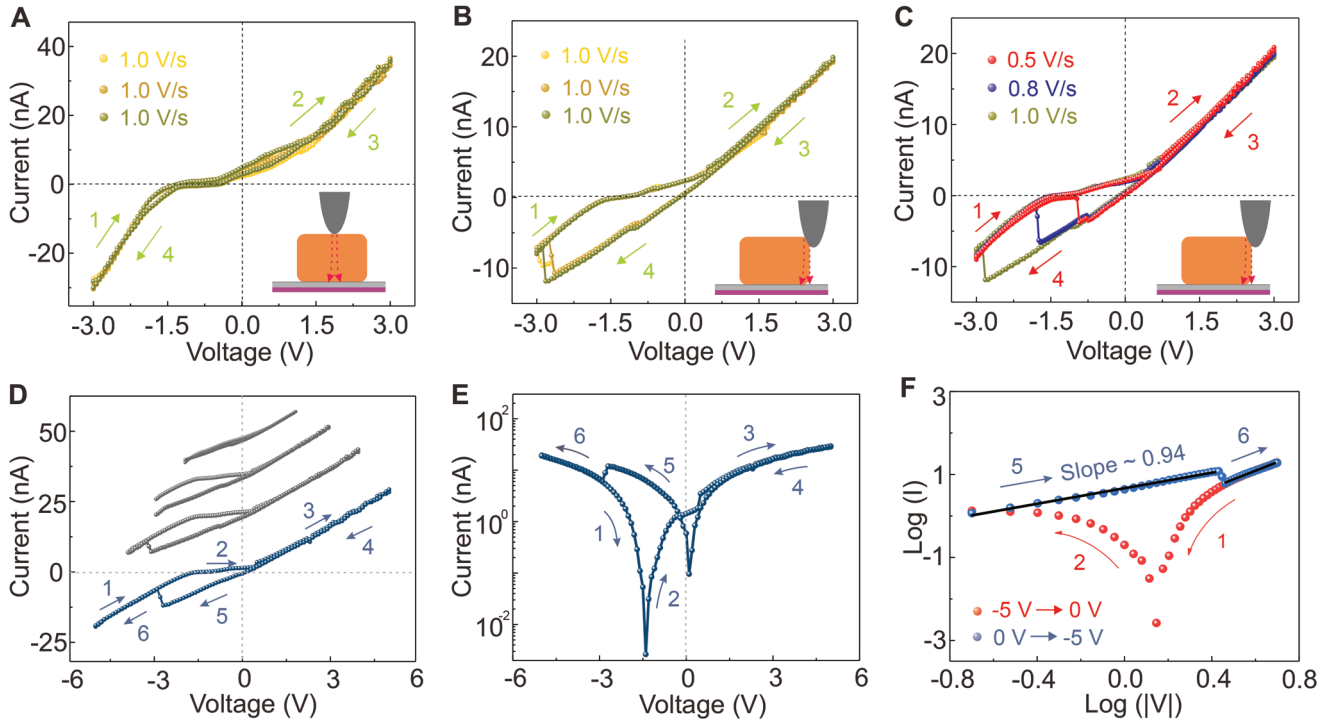

Figure 3. *I*–*V* curves of EGaIn–perovskite–graphene junctions upon light illumination with different contact geometries. The lateral dimension of the crystal was ≈100 µm. The numbers show the sequence of the voltage sweep process, and the solid arrows indicate the direction of the voltage sweep. A) Repeated *I*–*V* curves for the top-contact geometry. The inset is a simplified sketch of the top-contact geometry. The red arrows indicate the carrier's pathway. B) Repeated *I*–*V* curves for the edge-contact geometry. C) *I*–*V* curves at different sweep speeds for the edge-contact geometry. D) *I*–*V* curves under different voltage bias windows with the edge-contact geometry. The *I*–*V* curves are vertically shifted for clarification. Sweep speed: 1.0 V s^{-1}. E) The semi-logarithmic plot of *I*–*V* curves as the main curve presented in (D). F) Log (*I*)–log (*V*) curves with linear fitting at negative bias range as presented in (D).

formed. Normally, highly conducting paths can be formed via either defects or metal ion filaments.[38,45–49] Here, these highly conducting paths should be formed by the point defects near the crystal surface due to that: 1) the density of point defects on the crystal surface is much higher than that in the crystal interior,[29,50] and these defects with low active energy can migrate along the electric field to form a conductive filament;[51,52] 2) Unlike evaporated metal film, the free migrated metal ion is unavailable for both EGaIn and graphene in our case.[53]

At second, it is interesting that a reproducible conductance switch behavior was observed for the edge-contact geometry (Figure 3B). The conductance switch from a high conductance to a low conductance can be attributed to the rupture of defect filaments under reversed bias. It was reported that defects are thermodynamically stable and likely to be highly mobile at low activation energies.[12,52,54] Upon reversed voltage sweeping, the gradually increased field may trigger a reversed migration of defects and finally lead to the rupture of the conducting defect filaments, which is confirmed by the observation that the switching behavior disappears completely if the junction without undergoing a positive bias (Figure S5, Supporting Information).

Figure 3C shows that the triggered voltage for the conductance switch depends on the sweep speed of the applied voltage, that is, the trigger voltage shifts to a higher value as the sweep speed increases. This observation is reasonable since response time is required for defects migration to follow the variation of externally applied fields. Figure 3D shows that the switch behavior depends on the voltage sweeping window, that is, switch behavior disappears under a small sweep window, indicating that a sufficiently large bias voltage is needed to trigger the conductance switching. Figure 3E presents the semi-logarithmic plotted *I–V* curve. It shows that the current abruptly changes near 0.4 and −2.7 V, which corresponds to the required voltage for the formation and rupture of the conductive filaments, respectively. Figure 3F shows the logarithmic plotted *I–V* curves under negative bias. The slope of the linear fit line is close to 1.0 under the negative bias voltage (segment 5), confirming that conductive filaments are formed under positive bias and remained under a small negative bias.

It is noted that an obvious hysteresis effect (or switch) is observed under negative bias solely. It can be attributed to the 1) asymmetric contact-geometry, that is, a point-to-surface contact geometry is formed at the top contact interface but a surface-to-surface contact geometry is formed at the bottom contact interface for this sandwiched junction, which will result in an asymmetric electric field and thus asymmetric ion migration upon a polarized bias; 2) asymmetric energy landscape at the top and bottom contact interfaces, that is, Schottky contact is formed at the graphene/perovskite interface but an Ohmic contact is formed at the perovskite/EGaIn interface (Figure S6, Supporting Information). These asymmetric contact interfaces may lead to an asymmetric built-in field and asymmetric ion migration under different polarized biases.

2.3. Crystal-Sizes and Contact-Geometries Determined *I–V* Curves

To further understand the role of the pathway in determining carrier transport through microscale perovskite with varied sizes, we reduced the size of the perovskite microcrystals from ≈100 to ≈40 μm. Unlike large size crystal, the *I–V* curves of the small crystal demonstrate a strong rectification behavior with the top-contact geometry employing either bottom Au (Ag) electrode (**Figure 4**A and Figure S7, Supporting Information) or graphene electrode (Figure 4D). We attribute this strong rectification behavior to the energy landscape of the junction and ions migration. The energy band alignment of EGaIn–perovskite–Au junction under negative and positive bias voltages are shown in Figures 4B,C, respectively. It can be found that the carriers cannot be collected efficiently by the electrodes under a negative bias since both electrons and holes must overcome the energy barriers to reach the electrodes, which will result in a small current. More importantly, the electric field increases upon a bias due to the shrinking of crystal size, which will promote the migration of bromide ions, that is, considerable bromide ions with a small activation energy (≈0.2–0.6 eV)[51,55] will move to the positively biased bottom Au electrode (Figure 4B) leading to a compensating field, which in turn partly screens the external applied field. Contrary, the bromide ions will gradually diffuse from the interface under positive bias, and thus the carrier transport will not be blocked (Figure 4C).

Notably, the EGaIn–perovskite–graphene junction has similar energy band alignment to the EGaIn–perovskite–Au junction (see Figure 4B and Figure S6, Supporting Information). However, the carbon-based graphene substrate facilitates the adsorption of Br^-,[56] which will result in an enhanced ions accumulation at the perovskite/graphene interface. The accumulated negatively charged Br^- will repel the electrons from passing through the junction, leading to a stronger current suppression under negative bias. That is the reason why the EGaIn–perovskite–graphene junction shows a more pronounced rectification behavior compared to the EGaIn–perovskite–Au junction.

To support this ion migration hypothesis, additional experiments (X-ray photoelectron spectroscopy) were performed before and after the voltage application (Figure S8, Supporting Information), which verify the ion migration and accumulation of Br^-. Unlike traditional semiconductor junctions, the *I–V* characterization of perovskite junctions cannot be solely interpreted by the energy alignment of the junctions, since conduction filament may form in the perovskite junctions. With a close examination of Figure 4D, it can be found that the current linearly increases when the applied positive bias is larger than a threshold voltage (≈0.4–0.7 V), indicating that a conduction filament is formed when the applied positive bias is larger than the threshold positive voltage.[3,57] Through the fitting of log (*I*) versus log (*V*), it can be found that the slope is close to 1, which confirms the existence of conductive filaments (Figure S9, Supporting Information). It was reported that two kinds of point defects, V_{Br}^+ (vacancies) and Br′ (split interstitials), may form conduction filaments.[52] Considering that the density of V_{Br}^+ will greatly increase due to the Br^- migration but the density of Br′ is determined during the synthesis process of perovskite and normally do not change upon different bias, the dynamically formed filament should mainly consist of V_{Br}^+ under positive bias, as shown in Figure 4F.

To further understand the effect of electrode-contact geometries, half-enclosed contact geometry was generated by

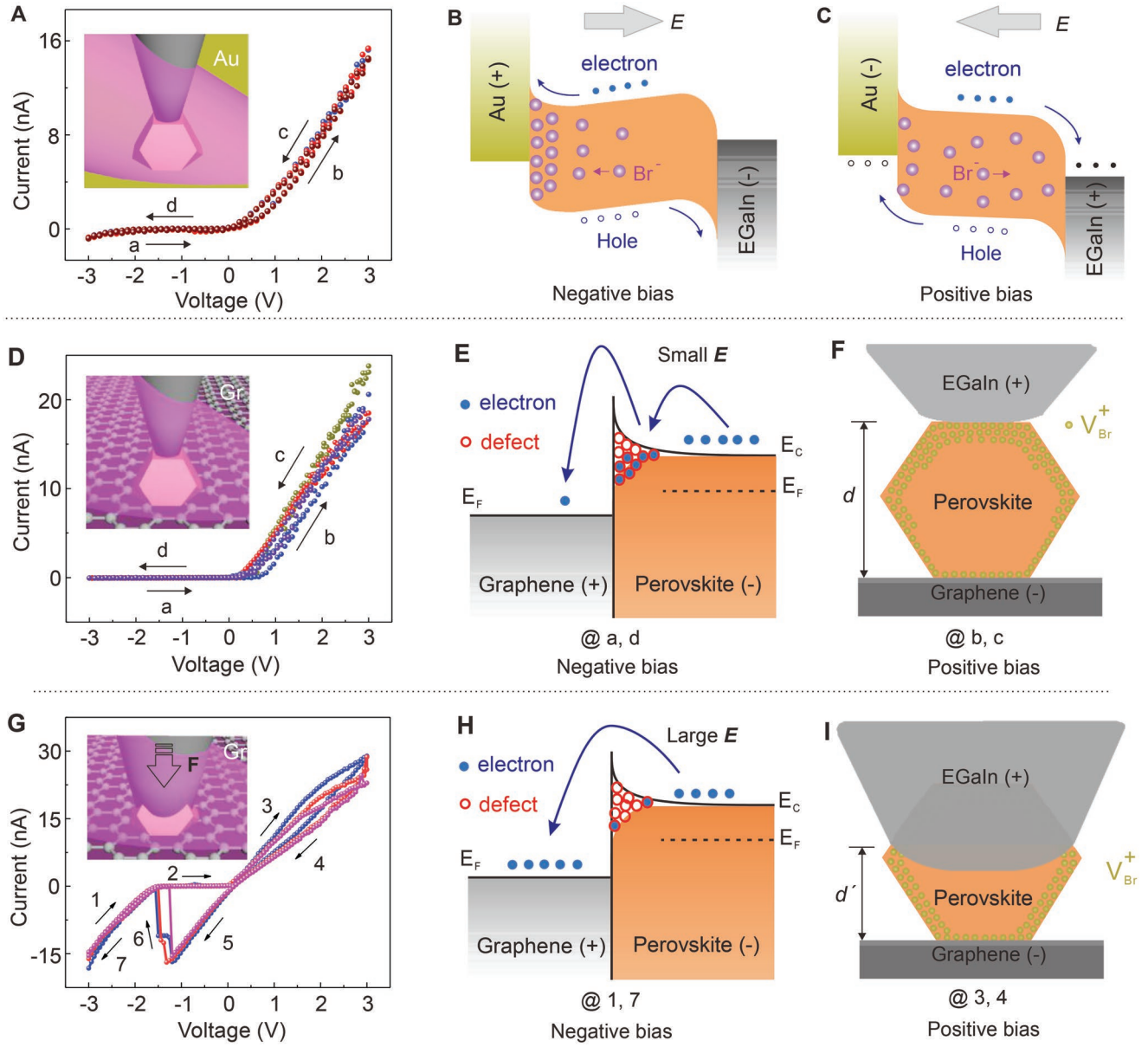

Figure 4. Carrier transport dynamics with different contact geometries and different bottom electrode materials. The lateral dimension of the crystal was reduced to ≈30 µm. A) Reproduced *I*–*V* curves of EGaIn–perovskite–Au junction with top contact geometry. The inset is the schematic diagram of the top contact geometry. The arrows indicate the sweeping direction of the voltage. B) The bromide ions accumulated at the Au/perovskite interface block the carrier transport under negative bias. C) The bromide ions diffused from the interface facilitate the carrier transport under positive bias. D) Repeated *I*–*V* curves of EGaIn–perovskite–graphene junction with the top-contact geometry. E) The Schottky barrier formed at the graphene/perovskite interface which assists in trapping carrier at the interface under negative bias. F) Schematic of the filament (V_{Br}^{+}) formation assisted by Br-migration which is promoted by the surface defects. G) Reduplicated *I*–*V* curves of EGaIn–perovskite–graphene junction with half-enclosed contact geometry. The inset is the schematic of the half-enclosed contact geometry. H) Schematic of electron transport across the Schottky barrier promoted by the increased active field due to the decreased distance (*d*′) between two electrodes. I) In the half-enclosed contact geometry, robust conductive filament (V_{Br}^{+}) is formed assisted by the ion migration with a reduced distance between two electrodes.

applying an appropriate push force on the substrate (Video S4, Supporting Information), in which the polyhedral perovskite crystal is half-enclosed by the adaptive deformed EGaIn electrode. Compared to the one with top-contact geometry, the half-enclosed junction shows a distinguishable *I*–*V* characterization (Figure 4G). At first, a conductance switch was reproducibly observed under negative bias (segment 6). We attribute the conductance switch to the rupture of the conductive filament formed under positive bias. As mentioned above, a filament consisting of V_{Br}^{+} will form under positive bias. Interestingly, this filament remains under a small reversed bias until suffering a relatively large negative bias (segment 5, Figure 4G). This reproducible rupture delay of the filament contrasts with the observation presented in Figure 4D in which the filament

breaks immediately even under a small positive bias. We attribute the rupture delay of the filament to the factors: 1) The contact area in half-enclosed contact geometry is much larger than the one in top-contact geometry, and 2) the distance between two electrodes (d') in half-enclosed contact geometry (Figure 4I) is shorter than the one (d) in top-contact geometry (Figure 4F). Thus, the filament formed in half-enclosed contact geometry is robust and can withstand a small reversed field without breaking. Notably, the switching behavior vanishes if the junction does not undergo a positive bias (Figure S10, Supporting Information), indicating that the positive bias promotes the formation of filaments once more.

At second, it is interesting to find that rectification behavior breaks down in the half-enclosed geometry. In other words, the negative current increases under a relative larger negative bias ($V_b < -1.5$ V) with the half-enclosed contact geometry (segments 7, Figure 4G), contrary to the observation with the top-contact geometry (Figure 4D) in which the current is completely suppressed under the whole negative bias window (−3, 0 V). This observation cannot be interpreted by the ion migration mechanism anymore, since the ion migration will be promoted in the size-reduced crystal, leading to a more pronounced rectification behavior. Therefore, we argue that this rectification behavior may rely on additional mechanism beyond the ion migration mechanism.

To understand the intrinsic mechanism for the breakdown of rectification, the following factors should be further taken into consideration: 1) the energy landscape of the interface which may result in carrier trapping events at the interface. It can be found that a Schottky contact is formed at the graphene/perovskite interface but an Ohmic contact is formed at the perovskite/EGaIn interface determined by the energy alignment between them (Figure S6, Supporting Information). The electrons may be trapped by the surface defects at the perovskite/graphene interface (Figure 4E); 2) Carrier trapping events determined by the surface defects. The large number of carriers will transport along the crystal surface in the half-enclosed geometry due to the shrinking of the crystal-size (increased surface-to-volume ratio), and thus the photoexcited carriers will encounter amount of surface defects, which will lead to serious carrier trapping events. Both interface carrier trapping and pathway carrier trapping events will result in a suppressed current under negative bias.

Upon a compression force, the tip of EGaIn electrode is dented to form a half-enclosed contact with perovskite microcrystals, and thus the electric field (E) strength will increase due to the decreasing of the distance (d') between two electrodes. The increased field will supply additional energy for electrons to overcome the Schottky barrier at the interface and thus be effectively collected by the graphene electrode under negative bias (Figure 4H). Additional to the detrapping of the carriers at the interface, the electrons trapped in the pathway may also escape from the trap center upon an increased field. Both will lead to the increase of current, resulting in the breakdown of the current suppression under a relatively larger negative bias.

2.4. Photoluminescence Spectra

To confirm that the defects distribution is inhomogeneous and ion migration truly occurs upon a bias voltage, the photoluminescence (PL) spectra were measured. Significant differences are observed in the PL spectrum near the vertical edge and surface center regions, especially after voltage applying to the perovskite crystal. **Figure 5**A is the optical image of the perovskite microcrystal before applying a bias voltage and Figure 5B is the PL intensity map collected from the white box area as marked in Figure 5A. It can be found that the PL intensity in the edge regime is much higher than the one in the surface center. It is reported that PL emission in $MAPbBr_3$ single crystals is related to defects because defects benefit charge carrier trapping and recombination leading to an enhanced PL emission.[58,59] Since the effective PL regime can be as deep as micrometers,[58] Figure 5B confirms that the defects density near edge is higher than the one in the crystal interior. Figure 5C shows the PL spectrum with normalized intensity collected from the three points as marked in Figure 5B before applying a voltage. It can be found that the maximum shifting of the PL peak position is quite small (0.7 nm) for the three points.

Figure 5D is the optical image of the perovskite microcrystal adhered to the EGaIn tip (right electrode) and Figure 5E is the PL intensity image after a negative bias voltage (4 V) was applied to the EGaIn electrode (≈0.1 V μm^{-1}). Unlike Figure 5B, the PL intensity gradually increases from right to left (from cathode to anode), and the left-most area (contact to the anode electrode) shows the maximum PL intensity. This observation is coherent with the previously reported observation,[59,60] in which the PL was enhanced in the bromide-rich regions when Br^- moves to the anode. With a close examination of the PL spectrum collected from three different points (marked in Figure 5E), it can be observed that the discrepancy of the PL peak positions increased significantly from 0.7 to 3.4 nm after applying a bias voltage. This increased shifting of the PL peak position can be attributed to reabsorption, geometry-dependent outcoupling efficiency, and polaron formation comprising Br-migration-induced distorted lattice and self-trapped carriers.[59,61] The observations presented in Figure 5E,F confirm that the ion migration truly occurs upon a bias voltage in the microscale crystals.

3. Conclusion

In summary, we demonstrated that the carrier transport through microscale perovskite single-crystal can be dramatically adjusted by adjusting the electrode contact-geometry in situ employing deformable liquid metal electrodes. The photocurrent exhibits a spike feature when carriers mainly pass through the crystal vertical surface. In contrast, the spike feature disappears when the carriers mainly pass through the crystal interior. With a further decrease in crystal size, strong rectification behavior was clearly observed for different substrates (graphene, Au, and Ag), and the rectification rate is the largest for the graphene substrate. Interestingly, this rectification broke down and a memristor behavior appeared upon a half-enclosed contact geometry. Assisted by the PL measurement, I–V measurement with varied bottom electrode materials, and photoelectron spectroscopy measurement, it is revealed that these observations originate from the inhomogeneous distribution

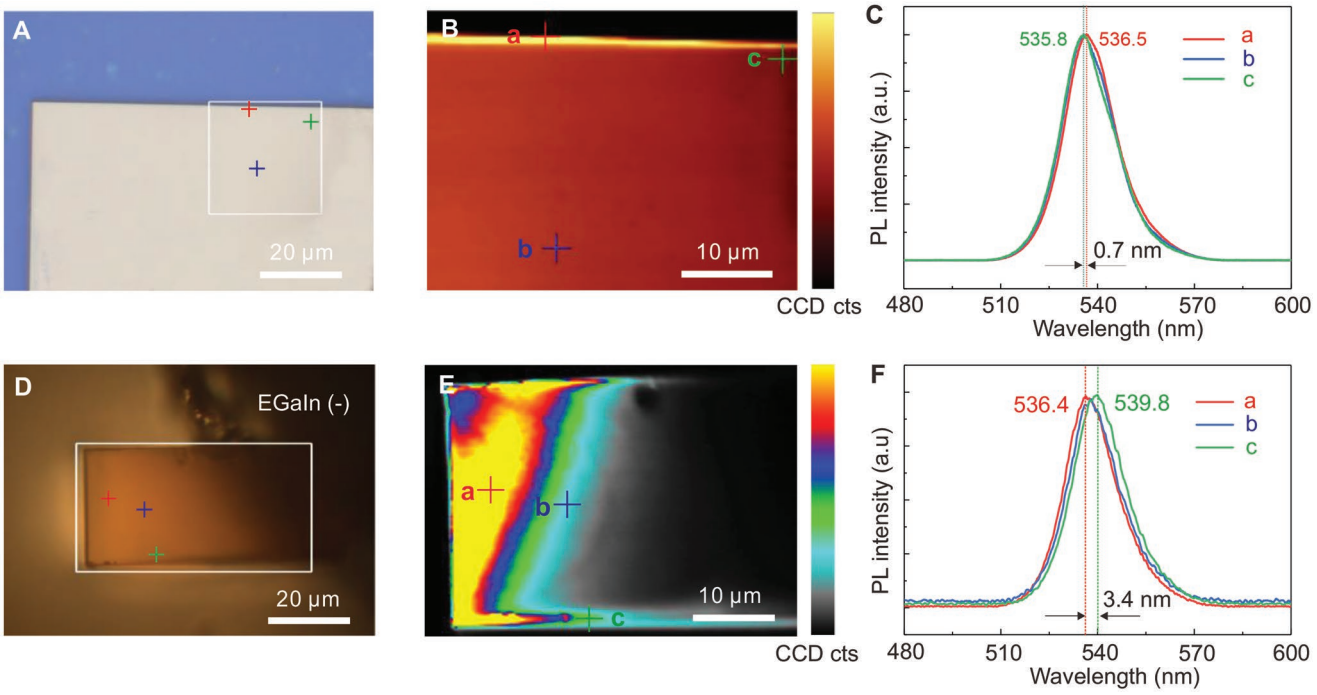

Figure 5. Optical imaging and PL characterization of a perovskite microcrystal before and after applying a bias voltage. A) Microscopic imaging of pristine perovskite microplatelet. B) The PL intensity map (main peak 536 nm) obtained from the white square area as presented in "a". C) The PL spectrum with normalized intensity obtained from the three points as marked in (B). The shifting of the PL peak position is 0.7 nm for the three points. D) Microscopic imaging of the EGaIn tip with an adhered perovskite microplatelet. E) The PL intensity map obtained from the white square area as presented in (D) after the voltage applied on the EGaIn–perovskite–graphene junction. F) The PL spectrum with normalized intensity obtained from the three points as marked in (E). The shifting of the PL peak position is 3.4 nm for the three points after applying a bias voltage.

of defects mediated by the crystal-size. It is confirmed that the defects density on the microscale crystal surface is much higher than the one in the crystal interior. The defects not only influence the carrier generation-recombination and carrier trapping–detrapping processes, but also assist the ion migration. Our study assists in establishing a platform for studying carrier transport through microscale crystals along the different pathways by the control of electrode contact-geometries and contact positions, showing the potential to integrate perovskite into all-soft electronic circuits with printing ink of EGaIn as deformable electrodes.

4. Experimental Section

Synthesis of Perovskite Microcrystals: The $MAPbBr_3$ microcrystals were synthesized according to previously reported procedures.[16] In brief, $MAPbBr_3$ solution was obtained by adding $PbBr_2$ to the mixed solution containing DMF and MABr and then heating at 70 °C for at least 1 h. DODB/GBL solution was obtained by mixing *n*-dodecylammonium bromide white powder (DODB) and gamma-butyrolactone (GBL) solvent. Subsequently, the $MAPbBr_3$ stock solution was rapidly injected into the DODB/GBL solution at room temperature, and the $MAPbBr_3$/DODB/GBL mixture was dropped onto the ITO substrate followed by a heating process. The obtained samples comprise isolated microwires and microcrystals. To synthesize perovskite, methylammonium bromide (MABr, ≥99.5%, MS301000-05) was obtained from Dyesol. *N*,*N*-dimethylformamide (DMF, 99.9%+, 494488-1 L), and lead bromide were purchased from Sigma-Aldrich. Dodecylamine and gamma-butyrolactone (GBL, ≥99%, B103608-500G) were purchased from Aldrich. The SEM image of finally synthesized perovskite crystals with different sizes and shapes can be found in Figure S2, Supporting Information.

Sample Characterization and the Electrical Measurement System: The morphology of the perovskite microcrystal and EGaIn tip was characterized by field-emission SEM (ZEISS Sigma 500). The PL spectrum was measured using a laser confocal Raman imaging spectrometer (WITec alpha 300R). The position and movement of the bottom graphene electrode were controlled by PiezoWalk actuators (PI, N-111, Germany) that can move continuously (maximum travel range of 10 mm) along the vertical direction with a resolution of 1 nm. The real-time current response upon light irradiation was recorded by a semiconductor analyzer (B1500A, KEYSIGHT). A semiconductor laser (MW-ZL-405, $\lambda = 405$ nm) was used as the illumination source, in which the power and the laser illumination frequency were controlled via a function generator (DS 435) and a buffer (BUF 634). The laser intensity is 13.9 mW mm^{-2} in the experiment if without a specific explanation.

Photoluminescence Measurement: The PL spectrum was measured using a laser confocal Raman imaging spectrometer (WITec alpha 300R, the wavelength of the laser is 488 nm). Two map modes, that is, peak position mapping mode and peak intensity mapping mode (main peak ≈536 nm) were used to characterize the perovskite crystal. Due to the factor that the microscale perovskite crystal is very easy to be damaged by the laser, thus the laser power was set to be quite small ≈0.03 mW. The image area is 25 μm × 25 μm, the measured point is 100 × 100 (i.e., spectra were collected at intervals of 250 nm), and the integration time is 0.01 s. The polarization voltage was set to 6 V and the duration time was 10 min before performing the PL.

Supporting Information

Supporting Information is available from the Wiley Online Library or from the author.

Acknowledgements

Z.Z. and Y.L. contributed equally to this work. The authors acknowledge the financial support from the National Key R&D Program of China (2021YFA1200103), the National Natural Science Foundation of China (91950116, 11804170, 61874167), the Natural Science Foundation of Tianjin (19JCZDJC31000, 19JCJQJC60900), and the National Research Foundation of Korea (NRF) grants (No. 2021R1A2C3004783).

Conflict of Interest

The authors declare no conflict of interest.

Data Availability Statement

The data that support the findings of this study are available in the Supporting Information of this article.

Keywords

carrier-pathway, charge trapping and detrapping, ion migration, liquid metal electrodes, perovskite microcrystals

Received: October 4, 2022
Revised: December 14, 2022
Published online: February 15, 2023

[1] Q. Dong, Y. Fang, Y. Shao, P. Mulligan, J. Qiu, L. Cao, J. Huang, *Science* **2015**, *347*, 967.
[2] Y. Bi, E. M. Hutter, Y. Fang, Q. Dong, J. Huang, T. J. Savenije, *J. Phys. Chem. Lett.* **2016**, *7*, 923.
[3] D. Shi, V. Adinolfi, R. Comin, M. Yuan, E. Alarousu, A. Buin, Y. Chen, S. Hoogland, A. Rothenberger, K. Katsiev, Y. Losovyj, X. Zhang, P. A. Dowben, O. F. Mohammed, E. H. Sargent, O. M. Bakr, *Science* **2015**, *347*, 519.
[4] S. D. Stranks, G. E. Eperon, G. Grancini, C. Menelaou, M. J. P. Alcocer, T. Leijtens, L. M. Herz, A. Petrozza, H. J. Snaith, *Science* **2013**, *342*, 341.
[5] U. K. Thakur, A. M. Askar, R. Kisslinger, B. D. Wiltshire, P. Kar, K. Shankar, *Nanotechnology* **2017**, *28*, 274001.
[6] H. Huang, H. Yan, M. Duan, J. Ji, X. Liu, H. Jiang, B. Liu, S. Sajid, P. Cui, Y. Li, M. Li, *Appl. Surf. Sci.* **2021**, *544*, 148583.
[7] Y. Lv, H. Tong, W. Cai, Z. Zhang, H. Chen, X. Zhou, *J. Alloys Compd.* **2021**, *851*, 156785.
[8] W.-J. Lee, H. J. Kim, J. Kang, D. H. Jang, T. H. Kim, J. H. Lee, K. H. Kim, *Annu. Rev. Mater. Res.* **2017**, *47*, 391.
[9] W. Xu, Y. Guo, X. Zhang, L. Zheng, T. Zhu, D. Zhao, W. Hu, X. Gong, *Adv. Funct. Mater.* **2017**, *28*, 1705541.
[10] C. Li, S. Tscheuschner, F. Paulus, P. E. Hopkinson, J. Kiessling, A. Kohler, Y. Vaynzof, S. Huettner, *Adv. Mater.* **2016**, *28*, 2446.
[11] W. Nie, J. C. Blancon, A. J. Neukirch, K. Appavoo, H. Tsai, M. Chhowalla, M. A. Alam, M. Y. Sfeir, C. Katan, J. Even, S. Tretiak, J. J. Crochet, G. Gupta, A. D. Mohite, *Nat. Commun.* **2016**, *7*, 11574.
[12] Z. Xiao, Y. Yuan, Y. Shao, Q. Wang, Q. Dong, C. Bi, P. Sharma, A. Gruverman, J. Huang, *Nat. Mater.* **2015**, *14*, 193.
[13] E. J. Juarez-Perez, R. S. Sanchez, L. Badia, G. Garcia-Belmonte, Y. S. Kang, I. Mora-Sero, J. Bisquert, *J. Phys. Chem. Lett.* **2014**, *5*, 2390.
[14] T. Pang, R. Jia, Y. Wang, K. Sun, Z. Hu, Y. Zhu, S. Luan, Y. Zhang, *J. Mater. Chem. C* **2019**, *7*, 609.
[15] Y. Wang, X. Guan, W. Chen, J. Yang, L. Hu, J. Yang, S. Li, K. Kalantar-Zadeh, X. Wen, T. Wu, *ACS Appl. Mater. Interfaces* **2020**, *12*, 38376.
[16] Z. Zhao, W. Wang, X. Zhou, L. Ni, K. Kang, T. Lee, H. Han, H. Yuan, C. Guo, M. Wang, M. J. Ko, Y. Li, D. Xiang, *Nano Lett.* **2020**, *20*, 8640.
[17] V. Nandal, P. R. Nair, *ACS Nano* **2017**, *11*, 11505.
[18] Y. Zhao, W. Zhou, H. Tan, R. Fu, Q. Li, F. Lin, D. Yu, G. Walters, E. H. Sargent, Q. Zhao, *J. Phys. Chem. C* **2017**, *121*, 14517.
[19] A. Guerrero, J. You, C. Aranda, Y. S. Kang, G. Garcia-Belmonte, H. Zhou, J. Bisquert, Y. Yang, *ACS Nano* **2016**, *10*, 218.
[20] H. Lee, D. Ko, C. Lee, *ACS Appl. Mater. Interfaces* **2019**, *11*, 11667.
[21] M. H. Futscher, M. K. Gangishetty, D. N. Congreve, B. Ehrler, *ACS Appl. Electron. Mater.* **2020**, *2*, 1522.
[22] T. Cheng, G. Tumen-Ulzii, D. Klotz, S. Watanabe, T. Matsushima, C. Adachi, *ACS Appl. Mater. Interfaces* **2020**, *12*, 33004.
[23] P. Teng, S. Reichert, W. Xu, S.-C. Yang, F. Fu, Y. Zou, C. Yin, C. Bao, M. Karlsson, X. Liu, J. Qin, T. Yu, W. Tress, Y. Yang, B. Sun, C. Deibel, F. Gao, *Matter* **2021**, *4*, 3710.
[24] B. Murali, E. Yengel, C. Yang, W. Peng, E. Alarousu, O. M. Bakr, O. F. Mohammed, *ACS Energy Lett.* **2017**, *2*, 846.
[25] C. Stecker, K. Liu, J. Hieulle, R. Ohmann, Z. Liu, L. K. Ono, G. Wang, Y. Qi, *ACS Nano* **2019**, *13*, 12127.
[26] B. Wu, K. Fu, N. Yantara, G. Xing, S. Sun, T. C. Sum, N. Mathews, *Adv. Energy Mater.* **2015**, *5*, 1500829.
[27] Q. Dong, J. Song, Y. Fang, Y. Shao, S. Ducharme, J. Huang, *Adv. Mater.* **2016**, *28*, 2816.
[28] G. Grancini, V. D'Innocenzo, E. R. Dohner, N. Martino, A. R. Srimath Kandada, E. Mosconi, F. De Angelis, H. I. Karunadasa, E. T. Hoke, A. Petrozza, *Chem. Sci.* **2015**, *6*, 7305.
[29] Y. Lei, Y. Xu, M. Wang, G. Zhu, Z. Jin, *Small* **2021**, *17*, 2005495.
[30] W. Xu, G. Lei, C. Tao, J. Zhang, X. Liu, X. Xu, W.-Y. Lai, F. Gao, W. Huang, *Adv. Funct. Mater.* **2018**, *28*, 1802320.
[31] T. Wang, G. Lian, L. Huang, F. Zhu, D. Cui, Q. Wang, Q. Meng, C.-P. Wong, *ACS Appl. Mater. Interfaces* **2020**, *12*, 38314.
[32] S. J. Kim, J. Byun, T. Jeon, H. M. Jin, H. R. Hong, S. O. Kim, *ACS Appl. Mater. Interfaces* **2018**, *10*, 2490.
[33] J. H. Heo, D. H. Shin, S. H. Moon, M. H. Lee, D. H. Kim, S. H. Oh, W. Jo, S. H. Im, *Sci. Rep.* **2017**, *7*, 16586.
[34] A. Wan, L. Jiang, C. S. S. Sangeeth, C. A. Nijhuis, *Adv. Funct. Mater.* **2014**, *24*, 4442.
[35] X. Chen, H. Hu, J. Trasobares, C. A. Nijhuis, *ACS Appl. Mater. Interfaces* **2019**, *11*, 21018.
[36] R. C. Chiechi, E. A. Weiss, M. D. Dickey, G. M. Whitesides, *Angew. Chem., Int. Ed.* **2008**, *47*, 142.
[37] C. Shi, Z. Zou, Z. Lei, P. Zhu, W. Zhang, J. Xiao, *Sci. Adv.* **2020**, *6*, eabd0202.
[38] B. Ku, B. Koo, A. S. Sokolov, M. J. Ko, C. Choi, *J. Alloys Compd.* **2020**, *833*, 155064.
[39] M. Wang, S. Cai, C. Pan, C. Wang, X. Lian, Y. Zhuo, K. Xu, T. Cao, X. Pan, B. Wang, S.-J. Liang, J. J. Yang, P. Wang, F. Miao, *Nat. Electron.* **2018**, *1*, 130.
[40] J. Gong, H. Yu, X. Zhou, H. Wei, M. Ma, H. Han, S. Zhang, Y. Ni, Y. Li, W. Xu, *Adv. Funct. Mater.* **2020**, *30*, 2005413.
[41] H. Jin, E. Debroye, M. Keshavarz, I. G. Scheblykin, M. B. J. Roeffaers, J. Hofkens, J. A. Steele, *Mater. Horiz.* **2020**, *7*, 397.
[42] B. Wu, H. T. Nguyen, Z. Ku, G. Han, D. Giovanni, N. Mathews, H. J. Fan, T. C. Sum, *Adv. Energy Mater.* **2016**, *6*, 1600551.
[43] X. Cui, S. Yuan, H. Zhang, X. Zhang, P. Wang, L. Tu, Z. Sun, J. Wang, Y. Zhan, L. Zheng, *Appl. Phys. Lett.* **2017**, *111*, 233302.
[44] Q. Han, S. H. Bae, P. Sun, Y. T. Hsieh, Y. M. Yang, Y. S. Rim, H. Zhao, Q. Chen, W. Shi, G. Li, Y. Yang, *Adv. Mater.* **2016**, *28*, 2253.
[45] Z. Xiong, W. Hu, Y. She, Q. Lin, L. Hu, X. Tang, K. Sun, *ACS Appl. Mater. Interfaces* **2019**, *11*, 30037.

[46] S. Ge, X. Guan, Y. Wang, C. H. Lin, Y. Cui, Y. Huang, X. Zhang, R. Zhang, X. Yang, T. Wu, *Adv. Funct. Mater.* **2020**, *30*, 2002110.
[47] Y. Sun, M. Tai, C. Song, Z. Wang, J. Yin, F. Li, H. Wu, F. Zeng, H. Lin, F. Pan, *J. Phys. Chem. C* **2018**, *122*, 6431.
[48] S. Lee, H. Kim, D. H. Kim, W. B. Kim, J. M. Lee, J. Choi, H. Shin, G. S. Han, H. W. Jang, H. S. Jung, *ACS Appl. Mater. Interfaces* **2020**, *12*, 17039.
[49] T. Paul, P. K. Sarkar, S. Maiti, K. K. Chattopadhyay, *ACS Appl. Electron. Mater.* **2020**, *2*, 3667.
[50] D. Meggiolaro, E. Mosconi, F. De Angelis, *ACS Energy Lett.* **2019**, *4*, 779.
[51] M. Chen, X. Shan, T. Geske, J. Li, Z. Yu, *ACS Nano* **2017**, *11*, 6312.
[52] J. Choi, S. Park, J. Lee, K. Hong, D. H. Kim, C. W. Moon, G. D. Park, J. Suh, J. Hwang, S. Y. Kim, H. S. Jung, N. G. Park, S. Han, K. T. Nam, H. W. Jang, *Adv. Mater.* **2016**, *28*, 6562.
[53] Y. Han, C. Nickle, Z. Zhang, H. Astier, T. J. Duffin, D. Qi, Z. Wang, E. Del Barco, D. Thompson, C. A. Nijhuis, *Nat. Mater.* **2020**, *19*, 843.
[54] C. Eames, J. M. Frost, P. R. Barnes, B. C. O'Regan, A. Walsh, M. S. Islam, *Nat. Commun.* **2015**, *6*, 7497.
[55] L. McGovern, M. H. Futscher, L. A. Muscarella, B. Ehrler, *J. Phys. Chem. Lett.* **2020**, *11*, 7127.
[56] H. Li, L. Tao, F. Huang, Q. Sun, X. Zhao, J. Han, Y. Shen, M. Wang, *ACS Appl. Mater. Interfaces* **2017**, *9*, 38967.
[57] J. S. Han, Q. V. Le, J. Choi, H. Kim, S. G. Kim, K. Hong, C. W. Moon, T. L. Kim, S. Y. Kim, H. W. Jang, *ACS Appl. Mater. Interfaces* **2019**, *11*, 8155.
[58] J. Ding, Z. Lian, Y. Li, S. Wang, Q. Yan, *J. Phys. Chem. Lett.* **2018**, *9*, 4221.
[59] Y. Luo, P. Khoram, S. Brittman, Z. Zhu, B. Lai, S. P. Ong, E. C. Garnett, D. P. Fenning, *Adv. Mater.* **2017**, *29*, 1703451.
[60] Z. Zhang, R. Kang, P. Cheng, Z. Liu, Z. Zuo, *Adv. Opt. Mater.* **2021**, *9*, 2100850.
[61] K. Zheng, M. Abdellah, Q. Zhu, Q. Kong, G. Jennings, C. A. Kurtz, M. E. Messing, Y. Niu, D. J. Gosztola, M. J. Al-Marri, X. Zhang, T. Pullerits, S. E. Canton, *J. Phys. Chem. Lett.* **2016**, *7*, 4535.